Research Square

Preprints are preliminary reports that have not undergone peer review.
They should not be considered conclusive, used to inform clinical practice,
or referenced by the media as validated information.

Past Antarctic Ice Sheet dynamics and retreat thresholds in the Wilkes Subglacial Basin

Robert McKay

robert.mckay@vuw.ac.nz

Victoria University of Wellington https://orcid.org/0000-0002-5602-6985

Tina van de Flierdt

Imperial College London https://orcid.org/0000-0001-7176-9755

Nicholas Golledge

Victoria University of Wellington https://orcid.org/0000-0001-7676-8970

Molly Patterson

Binghamton University, SUNY https://orcid.org/0000-0002-5058-9269

Elizabeth Keller

Victoria University of Wellington https://orcid.org/0000-0002-9408-9215

Stephen Meyers

Georgia Grant

GNS Science https://orcid.org/0000-0002-2615-9322

Nikita Turton

University College Dublin

Rachel Allison

Imperial College London

Francisco Jimenez-Espejo

Spanish National Research Council https://orcid.org/0000-0002-0335-8580

James Marschalek

Imperial College https://orcid.org/0000-0003-2057-4012

Tim Naish

Victoria University of Wellington https://orcid.org/0000-0002-1185-9932

David Wilson

University College London https://orcid.org/0000-0003-2786-4688

Richard Levy

Earth Sciences New Zealand https://orcid.org/0000-0002-8783-0167

Gavin Dunbar

Victoria University of Wellington https://orcid.org/0000-0002-9871-4225

Nicholas Sullivan

Penn State University

Christina Riesselman
University of Otago https://orcid.org/0000-0002-2436-4306
Trevor Williams
International Ocean Discovery Program, Texas A&M University https://orcid.org/0000-0001-9204-2731
Laura De Santis
National Institute of Oceanography and Applied Geophysics - OGS https://orcid.org/0000-0002-7752-7754
Carlota Escutia
CSIC-UGR https://orcid.org/0000-0002-4932-8619

Article

Keywords:

Posted Date: November 13th, 2026

DOI: https://doi.org/10.21203/rs.3.rs-11452077/v1

License: This work is licensed under a Creative Commons Attribution 4.0 International License.
Read Full License

Additional Declarations: There is **NO** Competing Interest.

Past Antarctic Ice Sheet dynamics and retreat thresholds in the Wilkes Subglacial Basin

Robert McKay[1], Tina van de Flierdt[2], Nicholas Golledge[1], Molly Patterson[3], Elizabeth Keller[1,4], Stephen Meyers[5], Georgia Grant[4], Nikita Turton[6], Rachel Allison[2], Francisco J. Jimenez-Espejo[7], Jim Marschalek[2], David J. Wilson[8], Tim Naish[1], Richard Levy[1,4], Gavin Dunbar[1], Nicholas B. Sullivan[9], Christina Riesselman[10], Trevor Williams[11], Laura De Santis[12], Carlota Escutia[6]

(1) Antarctic Research Centre, Victoria University of Wellington, Wellington, New Zealand, (2) Imperial College London, London, SW7, United Kingdom, (3) Department of Geological Sciences, Binghamton University, Binghamton, United States, (4) Earth Sciences NZ, Lower Hutt, New Zealand, (5) Department of Geosciences, University of Wisconsin Madison, Madison, WI, United States, (6) UCD School of Earth Sciences, University College Dublin, Ireland, (7) Instituto Andaluz de Ciencias de la Tierra (IACT-CSIC), Armilla, Spain, (8) Department of Earth Sciences, University College London, London, United Kingdom, (9) Penn State University, State College, Pennsylvania, USA; (10) Departments of Geology and Marine Science, University of Otago, Dunedin, New Zealand, (11) College of Marine Science, University of South Florida, USA (12) Istituto Nazionale di Oceanografia e di Geofisica Sperimentale (OGS), Sgonico, Italy.

The Wilkes Subglacial Basin (WSB), the largest marine-based sector of the East Antarctic Ice Sheet (EAIS), contains 3-4 m sea level equivalent ice volume and is considered highly vulnerable to instability processes under future warming scenarios[1–3]. Loss of marine-based ice in WSB has been implied during Pliocene (5.3-2.6 Ma) interglacials when global temperatures were 2–3°C warmer and atmospheric pCO_2 exceeded ~400 ppm[4]. Ice

retreat in the WSB has also been suggested within the last 400 kyr under more modest warming, although the magnitude of ice loss relative to the Pliocene remains uncertain[5–8]**. Here, we present a continuous 6-million-year-long record of iceberg-rafted debris and geochemical provenance tracers sourced from the WSB, providing evidence for shifts in iceberg calving and subglacial erosion related to ice sheet dynamics. Climate and ice sheet modelling experiments reveal that, while the pacing of marine-based erosion and iceberg calving in WSB was consistently modulated in a near-linear manner by orbital forcing, expansive grounding-line retreat required crossing a critical atmospheric warming threshold when pCO_2 exceeded 400 ppm. Our results demonstrate non-linear behaviour in the WSB, whereby once a warming threshold is breached, accelerated basal ice flow, dynamic thinning and flotation of the ice margin at its present-day bathymetric high occurs - after which ice loss within the largest EAIS marine catchment becomes irreversible on multi-millennial timescales**.

Instabilities associated with the marine-based sectors of Antarctica's ice sheets represent the largest uncertainty in future sea level rise projections[2,9]. Specifically, concern over the potential contribution of the Antarctic Ice Sheet to future sea level rise, and its irreversibility, arises from the combined influence of increased ocean heat flux to the grounding lines of marine-terminating ice sheets[10] and the reverse-slope nature of Antarctica's continental shelves. This bathymetric configuration results in increased likelihood of a self-reinforcing process known as marine ice sheet instability driving accelerated grounding line retreat once a threshold is breached[11]. Today, marine-based ice constitutes 22.7 m of sea level equivalent (sle)[1], with upwelling of warm subsurface Circumpolar Deep Water already leading to thinning of buttressing ice shelves[10]. If sustained, ice shelf thinning or collapse could lead to dynamic inland thinning of glaciers, and ultimately accelerated and irreversible retreat of parts of the inland West Antarctic Ice Sheet (WAIS; 3.4 m sle)[12,13]. Indeed, paleoclimate data and

49 modelling have shown multiple cycles of growth and collapse of the WAIS during warmer
50 intervals of the last 5 million years[14,15]. However, the majority of marine-based ice (19.2 m
51 sle) is located in East Antarctica[1], around which the oceanic regime and offshore/subglacial
52 bathymetry is highly variable. Increased snowfall under a warming climate in East Antarctica
53 has resulted in mass balance gains in recent years[16], but individual drainage basins are thought
54 to be subject to dynamic feedbacks and tipping thresholds that could offset any mass gains
55 from precipitation[17].

56 The Wilkes Subglacial Basin (WSB) is one of the largest marine-based drainage systems of
57 the East Antarctic Ice Sheet (EAIS), containing 3-4 m sle of ice. Although a large portion of
58 this sector is located on a reverse-slope bed and therefore vulnerable to marine ice sheet
59 instability processes, it is currently stabilised by an ice plug that rests on a coastal topographic
60 ridge of bedrock that slows ice flow. This ice plug provides a buffer against increases in ocean
61 heat flux, raising the threshold of warming required to trigger the onset of runaway retreat[18].
62 Model sensitivity tests suggest that lowering the ice sheet elevation enough to reach flotation
63 in the vicinity of the coastal "plug" requires atmospheric surface warming of ~4˚C to enable
64 sufficient surface melting, and/or a dynamic glaciological response. This thinning is required
65 to reduce the plug's stabilising influence and trigger an accelerated response to ocean warming
66 and marine ice sheet instability[3,18]. In contrast, much of the West Antarctic Ice Sheet (WAIS)
67 and the Weddell Sea catchments of the EAIS (e.g. Recovery Basin) have wider and broader
68 continental shelves and are therefore more vulnerable to ocean warming.

69 Despite the stabilising influence of this coastal ice plug, previous provenance (detrital element
70 concentrations; Nd and Sr isotope compositions) and iceberg-rafted debris (IBRD) studies from
71 offshore Wilkes Land have inferred retreat of the marine-based WSB grounding line south of
72 its present position during both Pliocene and Pleistocene warm intervals, and perhaps as

recently as 120 ka BP[4,5,19,20]. Here, we compile the first continuous, high-resolution record of WSB ice sheet dynamical response from Integrated Ocean Drilling Program (IODP) Site U1361 spanning the past six million years, using new and existing IBRD and provenance datasets. Previous studies identified a strong astronomical pacing in this dataset at cycles of 20-100 kyr, with IBRD peaks occurring during deglaciation events[5,19,20], but were too short in duration to robustly identify low-frequency astronomically-influenced responses at multi-million-year timescales[21]. These longer-term "grand" cycles act to modulate the relatively higher frequency eccentricity (400 and 100 kyr), obliquity (40 kyr) and precession (23 and 19 kyr) cycles, and have been implicated from deep-sea isotope studies as drivers of long-term variability in carbon cycling and global ice volume throughout much of the Cenozoic[22–24].

Ice sheet dynamics and threshold behaviour of the Wilkes Subglacial Basin

IODP Site U1361 is located in 3454 m water depth on a continental rise levee system adjacent to the WSB[25] (Figures 1 and S1). Since the Late Miocene, sedimentation has been governed by a combination of pelagic biogenic deposition and suspension settling of non-erosive, turbid overspill of cascading dense water masses forming on the George V Land continental shelf[26]. The levee style architecture observed in seismic profiles indicates that most fine-grained terrigenous sediment at the site derives from the George V Land continental shelf and is transported to the site through the adjacent canyon[25,26]. The iceberg calving events proximal to the ice sheet margin are reflected by coarse-grained terrigenous detritus in the form of IBRD deposition during periods of ice sheet advance and retreat[5,19,20]. The age model is based on an integrated bio- and magneto-stratigraphy[27] (see Methods; Figure S2), with linear interpolation between paleomagnetic reversal tie-points. To avoid circularity in attributing shifts in ice dynamics to orbital forcing, we do not conduct orbital tuning and assume constant long-term sedimentation rates between the paleomagnetic tie points. A total of 1389 grain size samples

were measured from ~10-gram samples to obtain our IBRD Mass Accumulation Rate (MAR) record spanning the last 6 million years (see Methods), with a median sampling interval of 3.8 kyr. Previous work at this site has indicated that the >250 μm fraction contains a grain-size population with a coarse tail distribution consistent with deposition from ice rafting, and is distinct from the well-sorted, symmetrical fine sand distribution deposited by density currents or aeolian processes[19,28].

A total of 253 depths were analysed for Nd and Sr isotopes, as marine detrital sediment provenance tracers, compiled from new samples and existing studies[4,5,29] at a lower resolution than the IBRD data (see Methods). These tracers covary with high-resolution (~1.5 kyr sample spacing) continuous major elemental contents (measured by X-ray fluorescence scanner) sensitive to provenance (K/Ti) and productivity (Ba/Al) changes (Figure 2). Previous studies at Site U1361 show interglacial diatom-rich muds with high Ba/Al ratios and $^{87}Sr/^{86}Sr$ ratios of 0.715 to 0.723 and ε_{Nd} values of -9 to -11, consistent with enhanced erosion of mixed Ferrar Large Igneous Province (FLIP) and the Beacon Supergroup strata it intrudes[4,5] (Figure 1). The supply of sediments from FLIP and Beacon Supergroup strata is interpreted to represent migration of the erosive margin of the EAIS several hundred kilometres inland, where the presence of those lithologies has been inferred using geophysical data[4,5,30] (Figure 1). At other times, $^{87}Sr/^{86}Sr$ ratios of 0.712 to 0.753 and ε_{Nd} values of -10 to -20 are consistent with erosion of the lower Palaeozoic granitoids and metamorphic rocks which characterise most of the bedrock at the modern-day ice margin[4]. The Nd and Sr isotope compositions covary with K/Ti ratios (Figure 2 and Figure S3), highlighting that the isotopic shifts are associated with larger shifts in the bulk sediment composition being delivered from the adjacent continental shelf in cascading waters rather than a minor constituent being advected from further afield. Consequently, lower K/Ti is interpreted as an increase in the relative flux of basaltic material (Ti-enriched) derived from the FLIP, reflecting inland migration of the EAIS grounding line

or more efficient subglacial sediment transport to the ice margin[29]. Peak IBRD MAR values have previously been noted to coincide with higher ε_{Nd} values and lower K/Ti ratios, indicating peak iceberg discharge during onset of periods with enhanced ice sheet erosion within the WSB[5,29]. However, not all IBRD comes from the WSB, with $^{40}Ar/^{39}Ar$ hornblende ages suggesting some input from the Victoria Land coast and even West Antarctica[31]. A recent comparison of Ross Sea versus Wilkes Land IBRD records indicates that the West Antarctic Ice Sheet was much more sensitive to higher frequency orbital forcing than the WSB[32]. Given the higher-frequency pacing of the Ross Sea IBRD record, the rarity of hornblende grains (<1%) in the U1361 IBRD fraction, and the consistency of most U1361 IBRD grains with strata within the WSB[31], the IBRD signal at U1361 is likely dominated by icebergs derived from the WSB—albeit with subordinate input from the Ross and Amundsen seas, as is the case today[32].

Provenance indicators (ε_{Nd}, $^{87}Sr/^{86}Sr$, K/Ti) and IBRD MAR in U1361 show the highest range from 6 to 2.6 Ma, implying enhanced variability of ice sheet erosion relative to later times – likely related to a retreated ice sheet margin inland during interglacials (Figures 1 and 2). Furthermore, peak ε_{Nd} values are -8 in the >2.6 Ma interval, indicating that inland erosion and ice loss during the Pliocene retreat events likely exceeded that of interglacials in the Pleistocene, for which peak ε_{Nd} values are generally lower than -10 (Figure 2). However, Pliocene retreat was not sufficient to erode large parts of the Adelie Craton to the south/west of the WSB, which would result in a reversal in the relationship between these provenance proxies[33] as observed during periods of EAIS retreat into the terrestrial hinterland during the Miocene[34]. Since 2.6 Ma, the intervals of lowest IBRD MAR amplitude are associated with the lowest variance in ε_{Nd} values, $^{87}Sr/^{86}Sr$ ratios and K/Ti ratios, implying prolonged periods of relatively subdued discharge of the ice sheet. However, peaks of IBRD return to similar (albeit slightly lower than) Pliocene levels between ~1.7 and 0.8 Ma (Figure 2a), and the IBRD and provenance tracers continue to show a consistent glacial/interglacial cyclicity. Although the

147 variance in these tracers increases slightly between ~1.7 and 0.8 Ma and it is a period of high
148 obliquity response (Figure 3, Figure 4b, c), the amplitude is much lower than the Pliocene.
149 These features imply that a warming climate into an interglacial period still results in enhanced
150 iceberg calving as well as faster basal sliding and erosion that propagated inland, and the higher
151 frequency response is greatest during periods of combined high obliquity and eccentricity, but
152 the magnitude of the response is not to the same extent as the Pliocene (Figures 3-4).
153 Comparison of ice sheet model experiments (Figure 1), IBRD/provenance tracers, and ice core
154 deflation data for the last interglacial period (~120 ka) shows that enhanced sliding at the bed
155 of the WSB will result in inland thinning and erosion further inland towards FLIP lithologies,
156 but this does not imply a southward migration of the grounding line[6,7]. Although the amplitude
157 of K/Ti variability decreases up-core, the glacial maxima values of ε_{Nd} are consistently low in
158 both the Pliocene and Pleistocene (averaging ~-14), suggesting the margin was eroding similar
159 regions during periods of maximum ice sheet extent over the past 6 Myr (Figures 1 and 2).
160 Combined, these data suggest that IBRD MAR and provenance tracers are capturing changes
161 in dynamic ice discharge rates and erosion at the ice margin, but do not provide a direct linear
162 scaling to either grounding line retreat or ice volume changes within the WSB catchment.

163 Mid-latitude sedimentary records indicating 20-30 m-amplitude sea level shifts sourced from
164 Antarctica in the Pliocene[35] suggest that the enhanced variability of IBRD and provenance prior
165 to 2.6 Ma implied by our data requires a mass contribution from the East Antarctic Ice Sheet,
166 consistent with a baseline shift in WSB retreat extent during interglacials. Atmospheric CO_2
167 concentrations during interglacials commonly exceeded 400 ppm prior to 2.6 Ma (Figure 2)[36],
168 with models showing this resulted in a warmer climate state that enhanced inland glacial
169 warming and basal sliding[37] (Supplementary Material; Figure S1). This in turn would lead to
170 deflation of the EAIS surface in the WSB to an extent that allowed flotation of the margin over
171 the coastal topographic ridge that currently buttresses this sector of the EAIS (Figure 1, panels

e-g). Once this flotation threshold was crossed, rapid inland retreat of the EAIS into the WSB would have been initiated via a range of glaciological feedbacks, including marine ice sheet instability (MISI) processes, enhanced by offshore warming of sea surface temperatures, as previously noted in diatom-based estimates at this site[38]. The baseline decreases in IBRD and provenance tracer variance after 2.6 Ma (Figure 2) suggests the threshold to trigger MISI into the WSB was not crossed as frequently after this time. Rather, proxy variability after 2.6 Ma suggests astronomical forcing resulted in a similar pacing of fluctuations of the ice margin on the outer continental shelf north of the modern grounding line, but with a more modest inland acceleration of ice streams during warm interglacials[5–8]. Such acceleration resulted in subglacial erosion within the WSB, but did not generate sufficient ice thinning to cause flotation of the grounding line at the coastal "ice plug" region that currently protects the WSB from widespread retreat through marine ice sheet instability[18] (Figures 1, panels b-d).

Orbital influences on the variability of ice rafting

Although the magnitude of the dynamic response of the ice sheet appears to shift at 2.6 Ma, there is a consistent response in the frequency of variability in the IBRD over the past 6 million years. Spectral analysis of the 6-million-year untuned IBRD MAR time series demonstrates strong power in the eccentricity and obliquity bands, with some precession-scale variability (Figures 3-4), although eccentricity is the most persistent frequency throughout the 6 Myr record. The IBRD MAR values are highest, and the IBRD MAR short-eccentricity-scale power is greatest, during ~2.4 Myr "grand cycle" nodes in the astronomical solution (Figure 4c-e). These nodes directly coincide with an enhanced ~100 kyr response in the LR04 benthic $\delta^{18}O$ stack, suggesting EAIS variability was large enough to be a major contributor to this geochemical, globally-integrated ice volume signal of the Pliocene (Figure 4c). This interpretation is supported by independently-derived sea level records[35]. The inverse

196 relationship between IBRD abundance and eccentricity amplitude (Figure 4d) provides a
197 compelling ground-truthing of an earlier hypothesis derived from deep sea isotopes, that
198 weaker eccentricity/precession forcing is less effective in forcing ice sheet melt[39]. This
199 hypothesis proposes that low eccentricity forcing resulted in prolonged periods of gradual ice
200 sheet growth across multiple precession cycles, which is supported by our observation of more
201 persistent background rates of iceberg calving during these eccentricity nodes. Consequently,
202 high abundance of IBRD is not a linear measure of past ice sheet collapse events, as large peaks
203 and background values appear to require the presence of substantive marine-based ice sheets
204 during preceding cold climate states.

205 The relationship of the IBRD to the benthic $\delta^{18}O$ stack only breaks down after 0.8 Ma (Figure
206 4c, d), which is interpreted as the Mid Pleistocene Transition and Northern Hemisphere Ice
207 Sheet glaciation dominating the ice volume component of the $\delta^{18}O$ stack after that time.
208 Obliquity is a subordinate signal in the U1361 IBRD data but has distinct ~0.5 Myr intervals
209 of increased power centred on ~1.7 Ma and 3.8 Ma. These intervals also coincide with
210 enhanced 40 kyr power in the astronomical solution[21] and the $\delta^{18}O$ stack[40] (Figure 3 and Figure
211 4a,b), indicating that the EAIS was directly responding to obliquity forcing to a magnitude that
212 influenced the signal in the far-field geochemical $\delta^{18}O$ stack throughout the entire Plio-
213 Pleistocene. However, the power of obliquity forcing in the astronomical solution does not
214 directly relate to the power of obliquity in the U1361 IBRD record, and the strongest peaks in
215 obliquity power coincide only when there is also high eccentricity forcing (Figures 3 and 4).

216 **Insolation driven surface warming threshold for WSB deglaciation**

217 Our results highlight that although the dynamic response of the WSB ice sheet to orbital
218 forcing is highly predictable over the past 6 million years, the influence of the orbital
219 configuration on the magnitude of WSB ice sheet retreat is non-linear and highly dependent

on atmospheric CO_2 boundary conditions. We hypothesize that periods of low eccentricity, which modulates the amplitude of precession, largely prevent the surface energy balance from reaching a threshold required to warm the ice sheet sufficiently to enhance ice sheet flow and cause deflation of the coastal part of the WSB when atmospheric CO_2 was less than 400 ppm (Figure 1). This scenario would prevent flotation and crossing of a critical threshold that would otherwise enhance sensitivity of the WSB to incursions of warm oceanic water regulated by obliquity[23] and trigger MISI processes that would widely deglaciate the WSB. In contrast, the high obliquity response of IBRD MAR during the combination of high obliquity and eccentricity forcing (every ~2.4 Myr) implies that eccentricity is modulating the response of the EAIS in the WSB to obliquity forcing throughout the entire record (Figure 3). Between 2.6 - 0 Ma, the highest amplitude variance of IBRD and provenance indicators occurs during combined high variance in eccentricity and obliquity, most notably between 1.8 and 0.8 Ma, suggesting this orbital configuration was the most optimal to trigger dynamic ice sheet responses when CO_2 remained below ~280-300 ppm during interglacials (Figure 2). However, the provenance indicators show that this variability was more muted after 2.6 Ma, compared to earlier times. This shift suggests that the combination of orbits promoting elevated summertime insolation at high southern latitudes and high CO_2 during interglacials (>400 ppm) was a prerequisite for initiating enough surface warming and dynamic ice sheet thinning to more regularly trigger a larger scale retreat in the WSB during the Pliocene.

To test the above hypothesis, we ran a series of sensitivity tests with an intermediate complexity Earth system model under a range of orbital configurations at both 280 and 400 ppm atmospheric CO_2. These indicate that while all scenarios show elevated atmospheric temperatures of ~2 ºC in the coastal WSB region, it is the combined high obliquity and eccentricity (perihelion) orbits that result in ~3ºC mean annual surface atmospheric temperature anomalies over the WSB under 400 ppm scenarios (Figure 5). However, in the

280 ppm atmospheric CO_2 scenarios, only the combined high-obliquity, high-eccentricity orbit (summer at perihelion) promotes any significant mean annual surface warming. Although this warming is lower in magnitude, it helps explain the frequency and higher amplitude response to IBRD and provenance indicators between 1.8 and 0.8 Ma, when obliquity and eccentricity variance was high, and interglacial CO_2 values were ~280-300 ppm (Figures 2 and 3). We propose that this warming may have been significant enough to trigger a dynamic response of the EAIS outlet glaciers in the WSB, but it does not imply widespread inland retreat, as the ice sheet may have been more expanded during glacial states when CO_2 was ~180 ppm.

On its own, eccentricity contributes very little power to insolation variance, and its influence on the ice sheet mass balance likely results from non-linear processes including precession amplitude modulation. Consequently, the dominance and persistence of eccentricity forcing on the IBRD record in the higher atmospheric CO_2 conditions prior to 2.6 Ma requires an explanation. Our model tests suggest this feature can be explained in the context of CO_2 ranging from ~280 ppm during glacial periods and ~400 ppm during interglacials (Figure 2). Under a 280-ppm scenario (e.g. Pliocene glacial states), low eccentricity orbital states produce neutral to negative temperature anomalies during both aphelion and perihelion, resulting in a prolonged cooling that allows ice sheet growth to occur at a ~100 kyr pacing (Figure 5). Consequently, the magnitude and pacing of the IBRD in the Pliocene is modulated by the precondition of requiring a relatively large marine-based ice sheet forming during glacial periods every 100 kyr. This interpretation is supported by the antiphase relationship of IBRD MAR and the eccentricity orbital solution (Figure 4). The short duration intervals of enhanced obliquity forcing, when eccentricity variance was higher, can also be explained by negative temperature anomalies in 280 ppm climates during aphelion. During

these configurations, peak cooling and glacial growth phases will occur during low obliquity configurations - which occur when obliquity variance is highest (Figure 3 and Figure 5). This glacial growth would be countered 20 kyr later by warmth and retreat, as obliquity reached its highest tilt configuration (Figure 5). In all our model scenarios, as atmospheric CO_2 rose above 400 ppm, large positive surface temperature anomalies occur in all orbital configurations (relative to 280 ppm atmospheric CO_2), with the largest occurring under the high eccentricity–high obliquity scenario. The increased amplitude of the provenance indicators suggests these surface warmings are significant enough to have promoted ice-sheet thinning, surface lowering, and flotation at the ice margin[3]. This floating marine margin is then subsequently exposed to enhanced ocean heat, amplifying subsurface ice–ocean feedbacks. While the magnitude of the temperature responses in these orbital experiments is broadly consistent with the thresholds proposed to trigger these processes[3], we note that important feedbacks that would further amplify the polar temperature response to higher pCO_2 are not accounted for in this model, including changes in adiabatic lapse rates due to lowering ice surface elevation, and ice sheet response/glacial meltwater feedbacks[41,42].

To assess the processes and timescales at which atmospheric temperature changes influence dynamic ice discharge, we examined the time-varying spatial attributes of our ice sheet simulations[43]. These experiments indicate that increases in air temperature result in rapid basal warming and surface melt feedbacks within a few hundred years, leading to dynamic thinning and enhanced discharge of grounded ice (Supplementary Material). Previous studies have also shown that higher precipitation rates under warmer climates[44], as well as thermal ice softening[45], can also result in enhanced ice discharge. Our data-model comparisons indicate that a high-eccentricity/high-obliquity configuration and 400 ppm atmospheric pCO_2 climate state are significant enough to atmospherically warm the ice sheet to an extent that enhanced

glacial flow/inland thinning is initiated, and offshore warming is significant enough to further enhance ice sheet melt and thinning as the grounding line passes into the coastal bathymetric ridge (ice plug) region. Once retreat from this pinning point is triggered, non-linear glaciological feedbacks (including MISI) lead to a rapid self-sustained retreat[18] that is irreversible on multi-millennial timescales.

Although Earth's orbital eccentricity is low today, atmospheric CO_2 now exceeds 429 ppm, which may result in higher levels of atmospheric warming over the WSB than seen in the Pliocene. Our results indicate that the triggering of marine ice sheet instability in the WSB reflects a clear threshold response to atmospheric warming. Consequently, although coastal to inland warming in East Antarctica may result in increased snow accumulation[16], our results indicate that it would be greatly outweighed by internal ice sheet feedbacks that result in enhanced glacial discharge and thinning from accelerating ice streams - eventually leading to triggering of marine ice sheet instability within the WSB and accelerated rates of sea level rise.

References

1. Fretwell, P. *et al.* Bedmap2: improved ice bed, surface and thickness datasets for Antarctica. *The Cryosphere* **7**, 375–393 (2013).
2. DeConto, R. M. *et al.* The Paris Climate Agreement and future sea-level rise from Antarctica. *Nature* **593**, 83–89 (2021).
3. Golledge, N. R., Levy, R. H., McKay, R. M. & Naish, T. R. East Antarctic ice sheet most vulnerable to Weddell Sea warming. *Geophys. Res. Lett.* **44**, 2343–2351 (2017).
4. Cook, C. P. *et al.* Dynamic behaviour of the East Antarctic ice sheet during Pliocene warmth. *Nat. Geosci.* **6**, 765–769 (2013).
5. Wilson, D. J. *et al.* Ice loss from the East Antarctic Ice Sheet during late Pleistocene interglacials. *Nature* **561**, 383–386 (2018).

6. Golledge, N. R. *et al.* Retreat of the Antarctic Ice Sheet During the Last Interglaciation and Implications for Future Change. *Geophys. Res. Lett.* **48**, e2021GL094513 (2021).
7. Sutter, J. *et al.* Limited Retreat of the Wilkes Basin Ice Sheet During the Last Interglacial. *Geophys. Res. Lett.* **47**, e2020GL088131 (2020).
8. Crotti, I. *et al.* Wilkes subglacial basin ice sheet response to Southern Ocean warming during late Pleistocene interglacials. *Nat. Commun.* **13**, 5328 (2022).
9. Masson-Delmotte, V. *et al.* Climate change 2021: the physical science basis. *Contrib. Work. Group Sixth Assess. Rep. Intergov. Panel Clim. Change* (Cambridge University Press, 2021).
10. Jenkins, A. *et al.* Observations beneath Pine Island Glacier in West Antarctica and implications for its retreat. *Nat. Geosci.* **3**, 468–472 (2010).
11. Thomas, R. H. & Bentley, C. R. A model for Holocene retreat of the West Antarctic Ice Sheet. *Quat. Res.* **10**, 150–170 (1978).
12. Rignot, E. *et al.* Four decades of Antarctic Ice Sheet mass balance from 1979–2017. *Proc. Natl. Acad. Sci.* **116**, 1095 (2019).
13. Rignot, E., Mouginot, J., Morlighem, M., Seroussi, H. & Scheuchl, B. Widespread, rapid grounding line retreat of Pine Island, Thwaites, Smith, and Kohler glaciers, West Antarctica, from 1992 to 2011. *Geophys. Res. Lett.* **41**, 3502–3509 (2014).
14. Naish, T. *et al.* Obliquity-paced Pliocene West Antarctic ice sheet oscillations. *Nature* **458**, 322–328 (2009).
15. Pollard, D. & DeConto, R. M. Modelling West Antarctic ice sheet growth and collapse through the past five million years. *Nature* **458**, 329–332 (2009).
16. Kolbe, M. *et al.* Atmospheric rivers and winter sea ice drive recent reversal in Antarctic ice mass loss. *Commun. Earth Environ.* **7**, 255 (2026).

17. Winkelmann, R., Garbe, J., Donges, J. F. & Albrecht, T. Mapping tipping risks from Antarctic ice basins under global warming. *Nat. Clim. Change* **16**, 341–3499 (2026) doi:10.1038/s41558-025-02554-0.
18. Mengel, M. & Levermann, A. Ice plug prevents irreversible discharge from East Antarctica. *Nat. Clim. Change* **4**, 451–455 (2014).
19. Patterson, M. O. *et al.* Orbital forcing of the East Antarctic ice sheet during the Pliocene and Early Pleistocene. *Nat. Geosci.* **7**, 841–847 (2014).
20. Bertram, R. A. *et al.* Pliocene deglacial event timelines and the biogeochemical response offshore Wilkes Subglacial Basin, East Antarctica. *Earth Planet. Sci. Lett.* **494**, 109–116 (2018).
21. Laskar, J. *et al.* A long-term numerical solution for the insolation quantities of the Earth. *Astron. Astrophys.* **428**, 261-285 (2004).
22. Palike, H. *et al.* The Heartbeat of the Oligocene Climate System. *Science* **314**, 1894–1898 (2006).
23. Levy, R. H. *et al.* Antarctic ice-sheet sensitivity to obliquity forcing enhanced through ocean connections. *Nat. Geosci.* **12**, 132–137 (2019).
24. Sullivan, N. B. *et al.* Obliquity disruption and Antarctic ice sheet dynamics over a 2.4-Myr astronomical grand cycle. *Sci. Adv.* **11**, eadl1996 (2025).
25. Escutia, C., Brinkhuis, H. & Klaus, A. Cenozoic East Antarctic ice sheet evolution from Wilkes Land margin sediments. *Proc. Integr. Ocean Drill. Program* **318**, (2011).
26. Donda, F., Brancolini, G., O'Brien, P. E., De Santis, L. & Escutia, C. Sedimentary processes in the Wilkes Land margin: a record of the Cenozoic East Antarctic Ice Sheet evolution. *J. Geol. Soc.* **164**, 243–256 (2007).

27. Tauxe, L. *et al.* Chronostratigraphic framework for the IODP Expedition 318 cores from the Wilkes Land Margin: Constraints for paleoceanographic reconstruction. *Paleoceanography* **27**, (2012).
28. McKay, R. *et al.* A Comparison of Methods for Identifying and Quantifying Ice Rafted Debris on the Antarctic Margin. *Paleoceanogr. Paleoclimatology* **37**, e2021PA004404 (2022).
29. Bertram, R. A. *et al.* Pliocene deglacial event timelines and the biogeochemical response offshore Wilkes Subglacial Basin, East Antarctica. *Earth Planet. Sci. Lett.* **494**, 109–116 (2018).
30. Ferraccioli, F., Armadillo, E., Jordan, T., Bozzo, E. & Corr, H. Aeromagnetic exploration over the East Antarctic Ice Sheet: A new view of the Wilkes Subglacial Basin. *Tectonophysics* **478**, 62–77 (2009).
31. Cook, C. P. *et al.* Glacial erosion of East Antarctica in the Pliocene: A comparative study of multiple marine sediment provenance tracers. *Chem. Geol.* **466**, 199–218 (2017).
32. Patterson, M. O. *et al.* Spatially variable response of Antarctica's ice sheets to orbital forcing during the Pliocene. *Nat. Geosci.* **19**, 182–188 (2026).
33. Halberstadt, A. R. W., Gasson, E., Pollard, D., Marschalek, J. & DeConto, R. M. Geologically constrained 2-million-year-long simulations of Antarctic Ice Sheet retreat and expansion through the Pliocene. *Nat. Commun.* **15**, 7014 (2024).
34. Pierce, E. L. *et al.* Evidence for a dynamic East Antarctic ice sheet during the mid-Miocene climate transition. *Earth Planet. Sci. Lett.* **478**, 1–13 (2017).
35. Grant, G. R. *et al.* The amplitude and origin of sea-level variability during the Pliocene epoch. *Nature* **574**, 237–241 (2019).
36. CENCO2PIP Consortium. Toward a Cenozoic history of atmospheric CO2. *Science* **382**, eadi5177 (2023).

391 37. Golledge, N. R. *et al.* Antarctic climate and ice-sheet configuration during the early
392 Pliocene interglacial at 4.23 Ma. *Clim Past* **13**, 959–975 (2017).
393 38. Taylor-Silva, B. I. & Riesselman, C. R. Polar Frontal Migration in the Warm Late
394 Pliocene: Diatom Evidence from the Wilkes Land Margin, East Antarctica.
395 *Paleoceanogr. Paleoclimatology* **33**, 76–92 (2018).
396 39. Raymo, M. E. The timing of major climate terminations. *Paleoceanography* **12**, 577–585
397 (1997).
398 40. Lisiecki, L. E. & Raymo, M. E. A Pliocene-Pleistocene stack of 57 globally distributed
399 benthic δ18O records. *Paleoceanography* **20**, 17 PP. (2005).
400 200510.1029/2004PA001071
401 41. Ashley, K. E. *et al.* Mid-Holocene Antarctic sea-ice increase driven by marine ice sheet
402 retreat. *Clim. Past* **17**, 1–19 (2021).
403 42. Suganuma, Y. *et al.* Antarctic ice-shelf collapse in Holocene driven by meltwater release
404 feedbacks. *Nat. Geosci.* **18**, 1216-1223 (2025).
405 43. Golledge, N. R. *et al.* Global environmental consequences of twenty-first-century ice-
406 sheet melt. *Nature* **566**, 65-72 (2019).
407 44. Winkelmann, R., Levermann, A., Martin, M. A. & Frieler, K. Increased future ice
408 discharge from Antarctica owing to higher snowfall. *Nature* **492**, 239–242 (2012).
409 45. Golledge, N. R. *et al.* The multi-millennial Antarctic commitment to future sea-level rise.
410 *Nature* **526**, 421–425 (2015).
411 46. Frederick, B. C. *et al.* Distribution of subglacial sediments across the Wilkes Subglacial
412 Basin, East Antarctica. *J. Geophys. Res. Earth Surf.* **121**, 790–813 (2016).
413 47. Studinger, M., Bell, R. E., Buck, W. R., Karner, G. D. & Blankenship, D. D. Sub-ice
414 geology inland of the Transantarctic Mountains in light of new aerogeophysical data.
415 *Earth Planet. Sci. Lett.* **220**, 391–408 (2004).

48. Ogg, J. G. Geomagnetic Polarity Time Scale. in *Geologic Time Scale 2020* 159–192 (Elsevier, 2020). doi:10.1016/B978-0-12-824360-2.00005-X.
49. Weaver, A. J. *et al.* The UVic earth system climate model: Model description, climatology, and applications to past, present and future climates. *Atmos.-Ocean* **39**, 361–428 (2001)

Figures

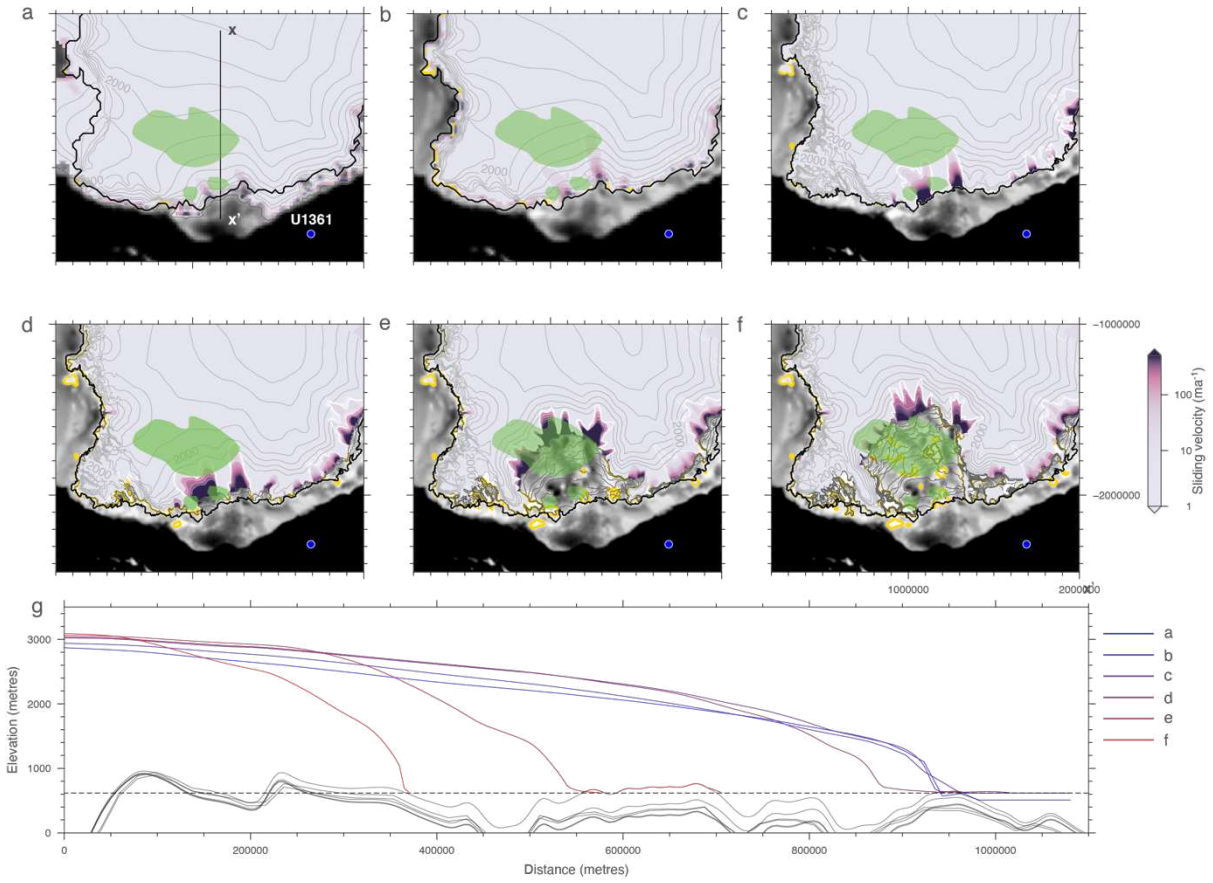
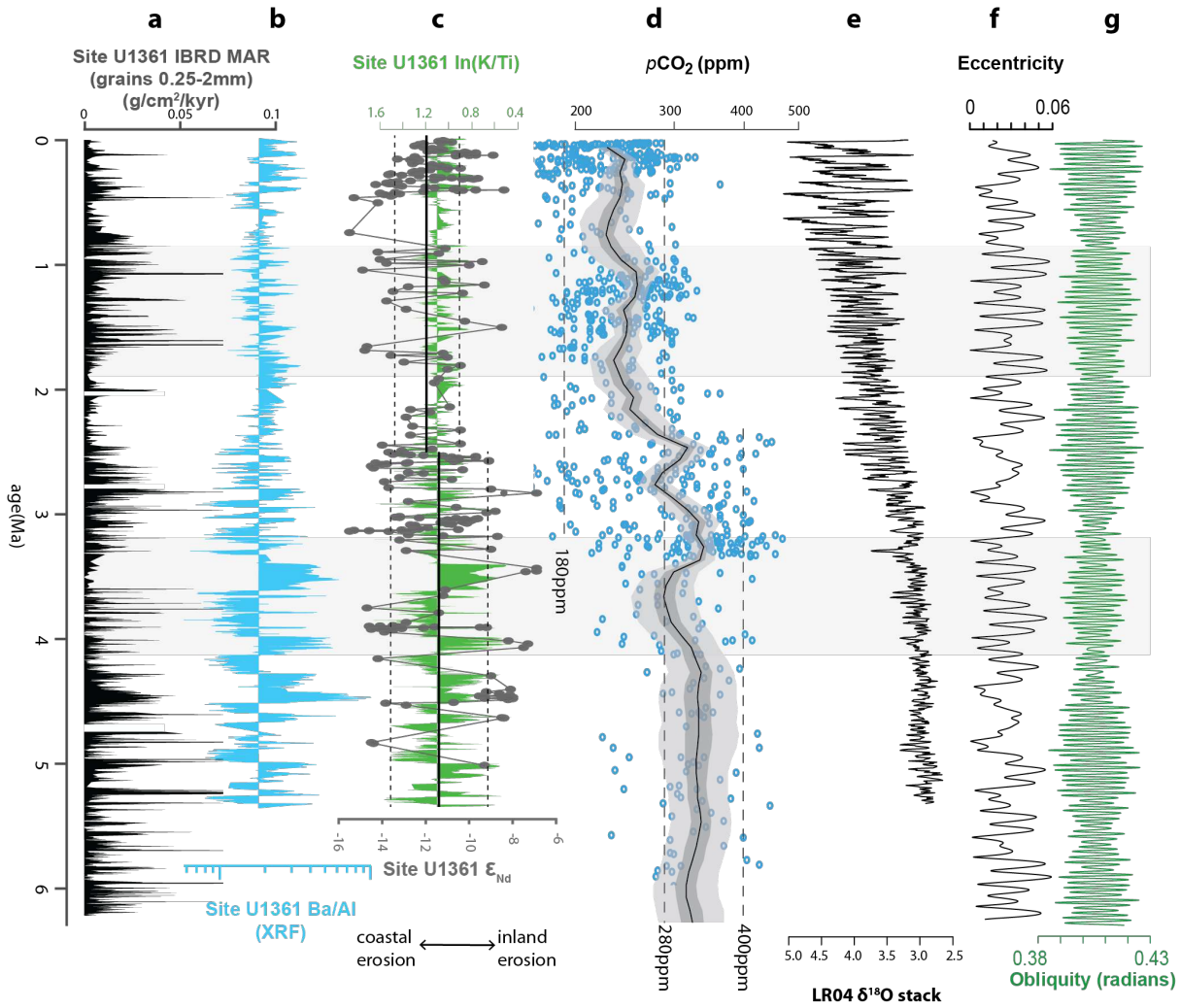
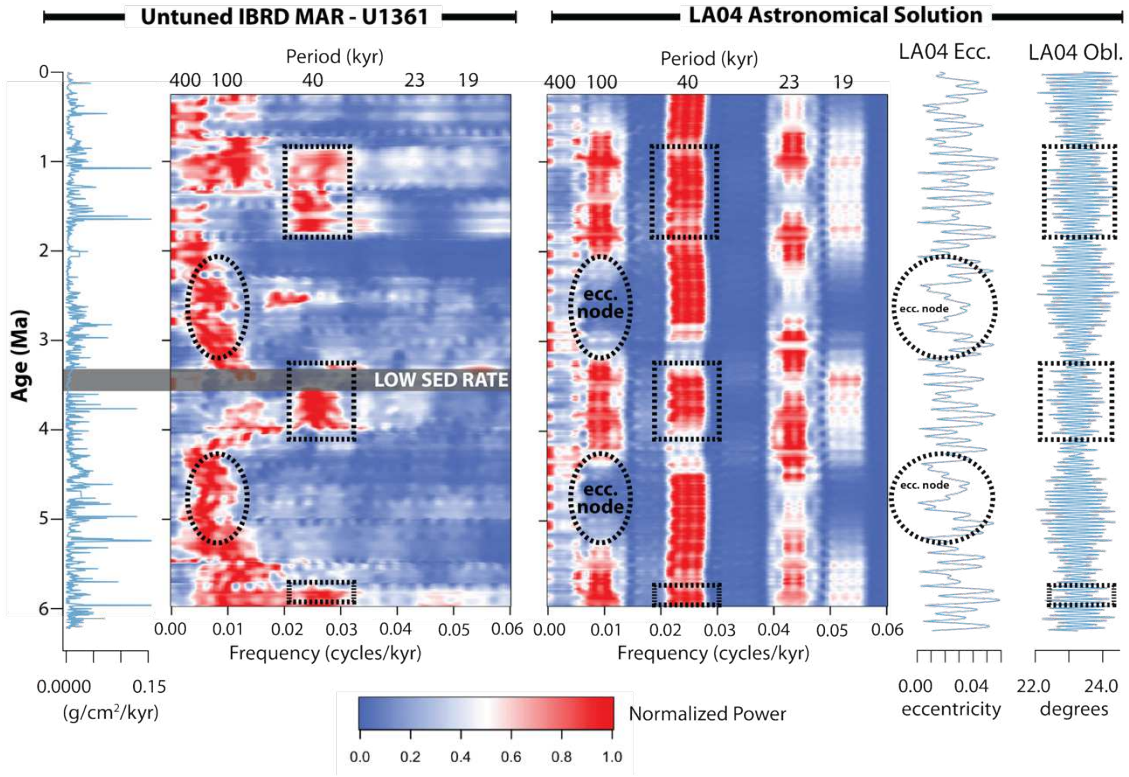


Figure 1: Modelled ice extent in the Wilkes Subglacial Basin. Grounded ice extent in the Wilkes Subglacial Basin sector of East Antarctica, proximal to U1361, simulated under climate states representative of: a, the Last Glacial Maximum; b, Present Day; c, the Last Interglacial; d--f, Simulated ice sheet extents at three stages of retreat under a constant warm Pliocene climate state[3,6,43]. Colour ramp shows basal velocity of the simulated ice sheet, highlighting areas where basal sliding most likely led to bedrock erosion and sediment transport. Profile line x-x' in panel a shows location of vertical ice sheet transects for each of the six modelled ice sheet extents in panel g. Green overlay with locations of Jurassic Ferrar Large Igneous Province (FLIP), as derived from airborne geophysics (after references [4,29,30,46,47]. Figure S1 provides a version of this figure without the FLIP overlay.



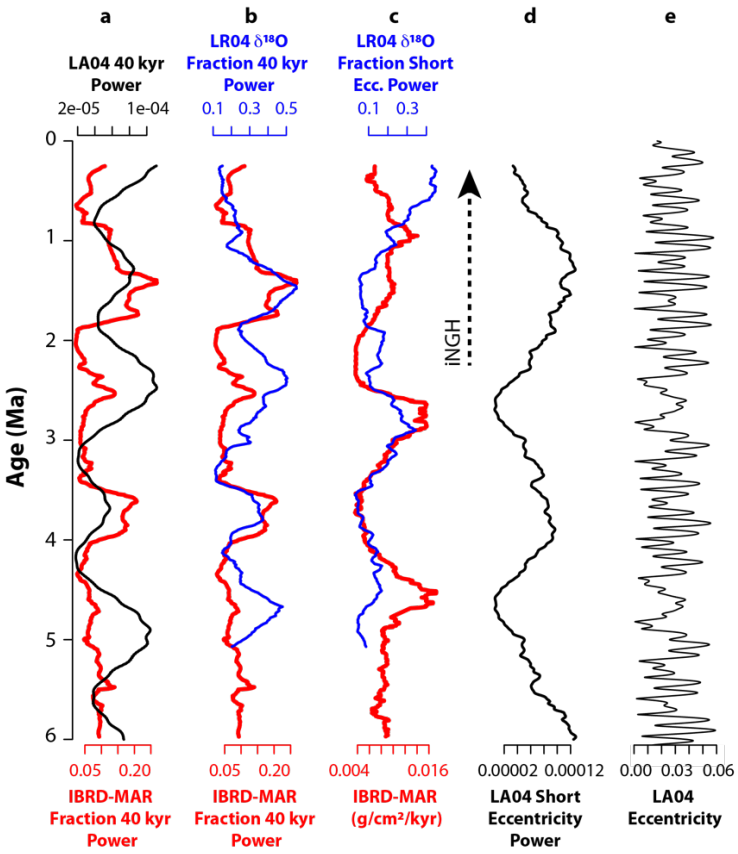
435

436 **Figure 2: Site U1361 proxy data and astronomical solutions plotted against age**
437 **(GTS2020[48]): a) Iceberg-Rafted Debris Mass Accumulation Rate (IBRD MAR); b) Ba/Al**
438 **XRF data (log scale); c) natural logarithm of K/Ti data (green line; scale inverted)**
439 **overlain with scatter plot of detrital ε_{Nd} values (dark grey dots and line). Vertical solid**
440 **black lines indicate mean ε_{Nd} values for 0–2.5 Ma (mean = −11.9 ± 1.5 (1σ)) and 5-2.5 Ma**
441 **(mean = −11.4 ± 2.2 (1σ)). Dashed black lines represent ±1 standard deviation bounds; d)**
442 **proxy-based estimates of pCO_2, with shading defining 25% (light grey) and 97.5% (dark**
443 **grey) percentile uncertainty ranges[36]; e) benthic $\delta^{18}O$ LR04 stack[40]; f) astronomical**
444 **solution for eccentricity[21]; g) astronomical solution for obliquity[21].**



445

446 **Figure 3: MTM time–frequency analysis results (500-kyr window, using three 2π prolate**
447 **tapers). Left: Time series of Iceberg-Rafted Debris Mass Accumulation Rate (IBRD**
448 **MAR) from IODP Site U1361. Centre left: Evolutive Power Spectral Analysis (EPSA),**
449 **showing normalized power for the untuned U1361 IBRD MAR data. Centre-right: EPSA,**
450 **showing normalized power for the eccentricity-tilt-precession (ETP) solution[21]. A linear**
451 **trend has been removed from each 500-kyr window, and power has been normalized such**
452 **that the maximum value in each window is unity. Right: the eccentricity and obliquity**
453 **(tilt) solutions[21].**



454

455 **Figure 4: Summary of astronomical-scale variability in Site U1361 IBRD MAR, the LR04**
456 **δ^{18}O benthic isotope stack[40], and the LA04 astronomical solution[21]. (a) Integrated**
457 **spectral power within the obliquity band for Site U1361 IBRD MAR and the LA04**
458 **solution. (b) Integrated spectral power within the obliquity band for Site U1361 IBRD**
459 **MAR and the LR04 stack. (c) Median IBRD MAR for Site U1361, and integrated spectral**
460 **power within the short eccentricity band for the LR04 stack. (d) Integrated spectral**
461 **power within the short eccentricity band for the LA04 solution. (e) The LA04 eccentricity**
462 **solution[21]. Panels a-d use a 500-kyr moving window. MTM spectral power integrations**
463 **use three 2π prolate tapers, and a linear trend is removed from each 500 kyr window.**
464 **Results for Site U1361 IBRD MAR and the LR04 stack are displayed as the fraction of**
465 **band power relative to all power at frequencies ≤ 0.1 cycles/kyr. iNHG = intensification**
466 **of Northern Hemisphere glaciation.**

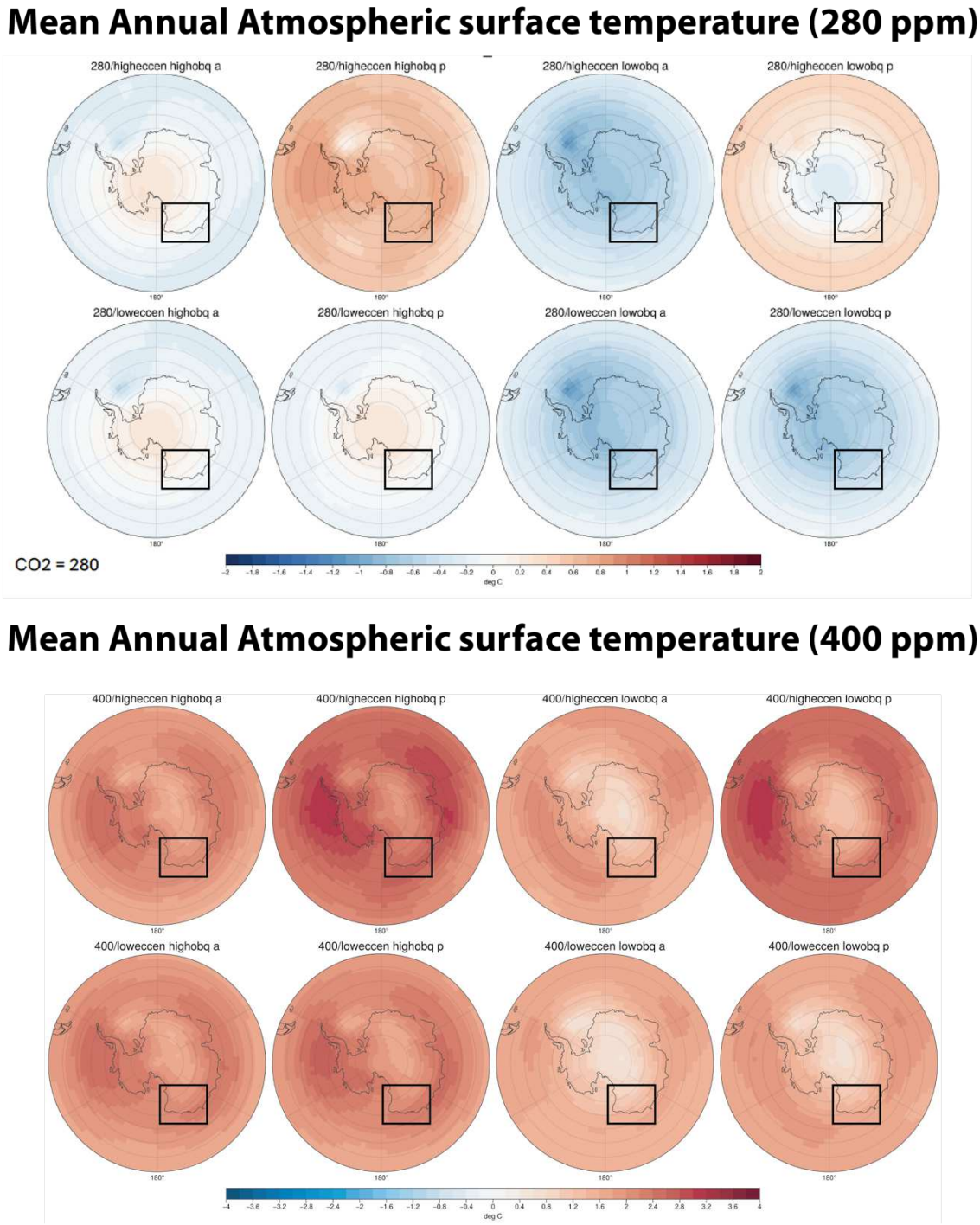


Figure 5: Earth system model (UVic ESCM v2.9[49]) sensitivity tests for a suite of differing orbital configurations. Orbital parameters (obliquity, eccentricity and longitude of perihelion) were set at eight different combinations ("lowobq" obliquity = 22.1, "highobq" = 24.5; "loweccen" eccentricity = 0.0034, "higheccen" = 0.058); Southern Hemisphere summer in perihelion ("p") = approximately present day (perihelion occurs

at 1 January) and Southern Hemisphere summer in aphelion ("a") = perihelion occurs at 1 July. Top 8 panels show annual mean surface atmospheric temperature anomalies at 280 ppm atmospheric CO_2 relative to a preindustrial control (modern orbital configuration with atmospheric CO_2 at 280 ppm). Black boxes show Wilkes Subglacial Basin sector in Figure 1. Bottom 8 panels show same tests under the various orbital scenarios, but with atmospheric CO_2 fixed at 400 ppm. Temperature anomaly is relative to a preindustrial control (modern orbital configuration with atmospheric CO_2 at 280 ppm).

Methods

IODP Site U1361 location and age model

IODP Site U1361 (64°14'42"S, 143°31'51.6"E) is located on the continental rise at 3454 m water depth approximately 315 km offshore Adélie Land, East Antarctica. The drill site is situated on the right (east) levee of the Jussieau submarine canyon system where the levee relief is ~195 m. U1361 penetrated to a depth of 388 m below seafloor, spanning the Middle Miocene to Pleistocene[25]. The age model for the U1361 record was developed through integration of biostratigraphic datums (diatom, radiolarian, calcareous nannofossils and dinoflagellate cyst) and the only revision to reference[27] is that the magnetic polarity zonation is tied to the 2020 geomagnetic polarity time scale (Figure S2)[48]. The average sedimentation rate is ~24.5 m/Myr, with no major shifts in sedimentation except for a short, condensed section of low sedimentation between 74.5 and 77.5 mbsf (3.33-3.596 Ma) where sedimentation rates drop to 8.5 m/Myr. Consequently, other than this one short interval, there are no large artifacts in our IBRD MAR calculations resulting in large pulses or drops in sedimentation rate, which is

483 evident when comparing the smoothed IBRD weight percent and IBRD MAR curves in Figure
484 S2.

485 **Iceberg-rafted debris**

486 A total of 1389 samples (20 cm^3 each) were analysed for grain size and IBRD (Supplementary
487 Table S1), of which 704 samples are new measurements for this study, 588 samples between
488 4.3 and 2.2 Ma were previously presented by Patterson *et al.*[19], and 97 samples between 0.5
489 and 0 Ma by Wilson *et al.*[5]. The 250 μm–2 mm (medium to very coarse sand) fraction was
490 used as the IBRD indicator, following established methods used at this site[5,19,28]. IBRD Mass
491 Accumulation Rate (IBRD MAR) was calculated using the method of ref[19]:

492 $$\text{IBRD MAR} = \text{CS \%} \times \text{DBD} \times \text{LSR}$$

493 where CS% is medium to very coarse (250 μm–2 mm) sand weight percent as a decimal
494 fraction, DBD is dry-bulk density (g/cm^3), and LSR is linear sedimentation rate (cm/kyr),
495 derived from the integrated bio-/magneto-stratigraphy[27,48] (Figure S2). The DBD for individual
496 IBRD samples was estimated via piecewise linear interpolation between the nearest dry bulk
497 density measurements (calculated using the Astrochron function 'accum').

498 For samples with mixed biogenic and terrigenous material, biogenic silica was removed from
499 the medium to very coarse sand fraction using 2 M NaOH. After dissolution, samples were dry
500 sieved at 150 μm, 250 μm, and 2 mm, then inspected for volcanic ash and authigenic minerals,
501 and if present the sample was excluded. Because biogenic material was removed and no
502 authigenic minerals or ash were present, CS% represents IBRD exclusively.

503 The use of IBRD abundance as a proxy for shifts in ice dynamics is well established in
504 Antarctica[50,51], including at Site U1361[5,19] which lies on the continental rise of Wilkes Land
505 underneath the Antarctic Slope Current – and acts to focus and transport icebergs over the site.

Determining the size fraction that contains exclusively IBRD can vary depending on the depositional setting and has to be considered in a site-specific context. Previous studies have indicated the sand fractions <250μm at Site U1361 could be influenced by downslope or aeolian processes[28,52], but the 250 μm-2 mm size fraction at U1361 has a distinct, poorly sorted "coarse tail" distribution that is distinct from the rest of the bulk sediment in the <250 μm fraction and is consistent with deposition from iceberg rafting[28]. IBRD primarily reflects melt-out from sediment-laden icebergs from outlet glaciers, though ice shelves likely influenced discharge. As Antarctic ice sheets lose about half their mass through iceberg calving, IBRD records in such Antarctic proximal locations are critical for understanding marine-based ice sheet dynamics – whereas sites north of the Antarctic Slope current may be more heavily influenced by sea surface temperature signals[53]. The U1361 record reveals a strong signal of orbital pacing of calving through the length of the record, indicating calving rates are not a random process. Since the Late Miocene, minimal surface melt means calving and ocean-driven melting dominated EAIS ablation[54–56]. While declines in IBRD MAR after 2.6 Ma may signal longer persistence of large fringing shelves, producing "cleaner" icebergs, it is important to note the buttressing effect of such ice shelves[57], and therefore a decline in IBRD is still consistent with our interpretations of changes in the rates of dynamical discharge. The bathymetric constraint of the continental rise means the directionality of the Antarctic Slope Current over U1361 remained stable over glacial to interglacial cycles, ensuring a consistent regional signal through time rather than current-driven shifts in single sources of the icebergs[58,59]. The site's deep-water, open-ocean setting prevents iceberg grounding, while the continuous presence of IBRD suggests the EAIS remained marine-terminating throughout, even during the largest retreat phases.

Earth system model

530 The UVic Earth System Climate Model (UVic ESCM) v2.9 was used to conduct sensitivity
531 tests for a suite of differing orbital configurations[49] (Figure 5). The UVic ESCM is an
532 intermediate-complexity Earth system model with coupled ocean, atmosphere, land and
533 biogeochemistry components, with 1.8º × 3.6º horizontal resolution and 19 ocean vertical
534 levels. The atmosphere is represented by an energy-moisture balance model with a single
535 vertical layer. The ocean model is a 3-D primitive equation general circulation model and
536 includes a thermodynamic-dynamic sea ice model. Orbital parameters (obliquity, eccentricity
537 and longitude of perihelion) were set at 8 different combinations (obliquity low = 22.1, high =
538 24.5; eccentricity low = 0.0034, high = 0.058); Southern Hemisphere summer in perihelion =
539 approximately present day (perihelion occurs on 1 January) and Southern Hemisphere summer
540 in aphelion = perihelion occurs on 1 July. Atmospheric CO_2 was fixed at 280 and 400 ppm for
541 each configuration. The Greenland and Antarctic Ice Sheets are static and are set to present-
542 day elevation and extent. The model was spun up for 10,000 years for each configuration, and
543 the last 100 years were used for analysis. The experiments were compared to a control
544 simulation with a present-day orbital configuration (obliquity = 23.44, eccentricity = 0.0167,
545 Southern Hemisphere summer at perihelion) with atmospheric CO_2 at 280 ppm.
546
547 **Ice Sheet Model experiments**
548
549 To investigate the mechanisms governing initiation and progression of ice margin retreat in the
550 Wilkes Subglacial Basin (Figure 1), we provide new analysis of the time-varying spatial
551 attributes of the modelled ice sheet from previous studies[3]. To reduce the dimensionality of the
552 system, and to capture changes taking place diachronously across the basin as the margin
553 migrates, we calculate spatial averages across a box of identical length to the profile line shown
554 in Figure 1, but with an expanded width that incorporates the full width of the retreated area.

555 The results reveal the relationship between the imposed atmospheric and oceanic forcing, and
556 the ice sheet response. a shows the step warming (dashed line) that is imposed in the "Pliocene"
557 simulation (red line) of Golledge et al. (2019)[43], compared to the "Modern" state (blue line).
558 Under the warmer atmospheric regime, temperatures at the bed of the ice sheet are also
559 markedly higher than under the modern state and initially rise to a maximum after
560 approximately 500 years before declining steadily for the remainder of the experiment (Figure
561 S4b). The abrupt warming imposed on the ice sheet results in an instantaneous increase in
562 surface melt rate (Figure S4c) that continues to rise for approximately 1000 years, due to the
563 melt—elevation feedback associated with surface lowering. During those first 500 years of
564 basal warming, basal melt rates rapidly increase (Figure S4d) and stay elevated for over 1000
565 years before decreasing in line with basal temperatures. The combined effects of surface and
566 basal melt lead to steady thinning of the ice sheet in the area (Figure S4e) with thinning rates
567 peaking during the first 400 years (Figure S4f). However, the net rate of thickness change also
568 incorporates dynamic effects (Figure S4g), which we calculate as the residual of the
569 accumulation and ablation terms:
570
571 Dynamic change = – dHdt + accum – smelt – bmelt
572
573 It is clear from the integrated horizontal ice flux (Figure S4h) that the area-averaged ice
574 discharge initially increases when most of the ice is still grounded, and several centuries before
575 the majority of ice in the area goes afloat (Figure S4, grey vertical bars). This enhanced
576 discharge is due to faster flow (Figure S4i,j) both at the surface and at the bed, and is possibly
577 related to the slightly greater proportion of basal sliding taking place under the warmer
578 conditions (Figure S4k). Ongoing thinning leads to a slow reduction in ice overburden pressure

579 (Figure S4l) that eventually reverses once basal melt rates and the rate of ice thinning have
580 declined (Figure S4, d,e).
581
582 In summary, retreat into the Wilkes Subglacial Basin appears to be controlled by an air
583 temperature-controlled velocity switch that triggers dynamic thinning and enhanced discharge
584 of grounded ice. Previous studies have also implicated greater surface precipitation rates under
585 warmer climates[44], as well as ice softening[45], and increased discharge, which may be the case
586 in our experiments too.
587
588 **XRF analysis**
589
590 The bulk major element composition was measured on cores from U1361A using an Avaatech
591 X-ray fluorescence core scanner at the IODP-Core Repository/Texas A&M University
592 laboratories (USA). Non-destructive XRF core-scanning measurements were performed at 10
593 kV in order to measure the relative content of elements. Measurements were acquired every 5
594 cm. In addition, 42 discrete samples were selected in a 20 m representative interval (47 to 67
595 mbsf; ~40-60 cm sampling intervals) for measurement by XRF, using pressed pellets prepared
596 by pressing about 5 g of ground bulk sediment into a briquette with boric acid backing. The
597 quality of the analysis was monitored with reference materials, showing high precision with 1
598 sigma 1.0-3.4% on 16 data-sets at the 95% confidence level. When compared, the Ba, K and
599 Al trends using both techniques are virtually identical and indicate that the obtained XRF-scan
600 data are robust and reliable.

601 It is well established that the K/Ti ratio in siliciclastic marine sediments can be used as a
602 terrigenous (land-derived) provenance proxy[60] and can even be used to discern ice-rafted-
603 debris in pelagic-rich sediment[61]. However, K concentration in deep-sea sediments is mainly

604 controlled by the presence of clay minerals, such as illite, or fine K-feldspar[62]. In low and
605 middle latitudes, the K concentrations may be controlled by chemical weathering intensity in
606 the sediment source area, with weathering products being progressively depleted in K[63], or
607 even by fluvial input[64]. Nevertheless, in an Antarctic setting subjected to extremely cold
608 climates which has been almost entirely covered by ice since the late Miocene, chemical
609 weathering or runoff are virtually absent[65]. On the other hand, Ti is a conservative element
610 with concentrations in fine fractions mainly associated with minerals such as biotite, ilmenite
611 or rutile. In different marine locations, Ti enrichments have been associated with the presence
612 of basaltic-derived sediments enriched in such minerals[66]. In the Wilkes Subglacial Basin,
613 basaltic material is mainly derived from the Ferrar Large Igneous Province (FLIP) that
614 includes a cover of high-Ti lavas of andesitic composition[67]. Based on these factors, the
615 measured K/Ti ratio is effective for reconstructing recurring changes in the basaltic
616 contribution to the terrigenous fraction.

617 **Neodymium and strontium isotopes**

618 Neodymium and strontium isotope measurements on the Site U1361 sediments were compiled
619 from Wilson *et al.*[5] (n = 85), Bertram *et al.*[20] (n = 70), Cook *et al.* 2014[4](n = 21), and Cook *et*
620 *al.* 2017[31] (n=10), complemented by additional, previously unpublished measurements[68] (n =
621 67). Different grain sizes were used (<63 μm, <150 μm and bulk samples), but investigation
622 of different size fractions from the same sample at this site revealed neodymium isotope
623 compositions either within, or close to within, error of each other[5,68]. There is therefore little
624 impact on the ε_{Nd} values from grain size choice at Site U1361. Although $^{87}Sr/^{86}Sr$ ratios are
625 influenced by grain size choices, any trends discussed here are primarily based on the Nd
626 isotope data.

627 Analytical procedures are also nearly identical across the different studies and the previously
628 unpublished data presented here[68]. Briefly, a leaching procedure was used to remove authigenic
629 ferromanganese mineral coatings, comprising an acid-reductive leaching solution containing
630 acetic acid and 0.02 M hydroxylamine hydrochloride. Biogenic opal was not removed. Leached
631 samples were then homogenised and digested, before Nd and Sr were isolated using ion
632 exchange chromatography. New samples analysed from the early Pliocene interval (104.06 –
633 106.53 mbsf) were processed through Tru-Spec resin (100 – 120 μm bead size) and Ln-spec
634 resin (50 – 100 μm bead size). For Plio-Pleistocene samples, the first Tru-Spec column was
635 substituted by Biorad cation exchange resin (200 – 400 μm mesh) to improve the yields of Nd
636 by preventing leakage of organics from the Tru-Spec resin[69,70]. The resin volume of the Ln-
637 spec columns was also reduced in the latter procedure (from 800 μl to 500 μl).

638 Neodymium isotope analysis was performed on a Nu Instruments multi collector inductively
639 coupled plasma mass spectrometer (MC-ICP-MS) in the MAGIC laboratories at Imperial
640 College London. Instrumental mass bias was corrected using the exponential law and a
641 $^{146}Nd/^{144}Nd$ ratio of 0.7219. A correction for direct ^{144}Sm interference was applied, although
642 amounts of ^{144}Sm were always negligible. Reported sample $^{143}Nd/^{144}Nd$ ratios are corrected
643 using the offset from batch or bracketing standards to the recommended JNdi-1 $^{143}Nd/^{144}Nd$
644 ratio of 0.512115[71]. Mean JNdi-1 values for the analytical sessions were 0.512111 ± 0.000012
645 (2.S.D., n = 24); 0.512119 ± 0.000013 (2.S.D., n = 21); 0.512132 ± 0.000013 (2.S.D., n = 28);
646 0.512113 ± 0.000015 (2.S.D., n = 10); 0.512101 ± 0.000012 (2.S.D., n = 30); 0.512107 ±
647 0.000012 (2.S.D., n = 34); 0.512099 ± 0.000011 (2.S.D., n = 32); 0.512116 ± 0.000016 (2.S.D.,
648 n = 30); 0.512140 ± 0.000011 (2.S.D., n = 24); 0.512100 ± 0.000014 (2.S.D., n = 13); 0.512089
649 ± 0.000019 (2.S.D., n = 13). External errors were calculated from the reproducibility of JNdi-
650 1 standard measurements for each given analytical session. Eleven replicates of standard
651 reference material BCR-2 were processed along with the unknown samples, with a mean

652 corrected $^{143}Nd/^{144}Nd$ ratio of 0.512639 ± 0.000017 (2 S.D., n = 28), in agreement with the
653 recommended value of 0.512638 ± 0.000015 (2 S.D)[72]. Procedural blanks were consistently
654 below 230 pg and mostly below 65 pg.

655 **Time-series analysis**

656

657 The Site U1361 IBRD MAR data were placed on an even sampling grid of 4 kyr prior to
658 spectral analysis, and the LR04 $\delta^{18}O$ benthic isotope stack[40] was placed on an even sampling
659 grid of 2.5 kyr, using piecewise linear interpolation (Astrochron function 'linterp')[73]. In both
660 cases the median sampling resolution was utilized to determine the appropriate interpolation
661 interval. Three data gaps were replaced with the mean values of the IBRD MAR data point
662 immediately above and below each gap. The LA04 solutions[21] utilize the nominal 1 kyr
663 sampling resolution provided by the original publication.

664

665 All MTM evolutive power spectral analyses use a 500 kyr moving window, with three 2π
666 prolate tapers (Astrochron function 'eha'; Figures 3 and 4). A linear trend is removed from
667 each 500 kyr window prior to estimating the spectrum. The power spectrum integrations
668 (Astrochron function 'integratePower'; Figure 4a-d) were conducted using the following
669 bandwidths: 0.02778-0.02174 cycles/kyr (obliquity), 0.007-0.012 cycles/kyr (short
670 eccentricity). A 500 kyr moving-window median IBRD MAR was determined for Site U1361
671 using the un-interpolated data (Astrochron function 'mwStats'; Figure 4c).

672

673 **Data availability**

674 All data used in this study are available in the supplementary data file.

675 **Methods references**

50. Weber, M. E. *et al.* Millennial-scale variability in Antarctic ice-sheet discharge during the last deglaciation. *Nature* **510**, 134–138 (2014).
51. Jasper, C. E. *et al.* A 3.3-Million-Year Record of Antarctic Iceberg Rafted Debris and Ice Sheet Evolution Quantified by Machine Learning. *Paleoceanogr. Paleoclimatology* **39**, e2024PA004897 (2024).
52. Passchier, S., Hansen, M. A. & Rosenberg, J. Quartz grain microtextures illuminate Pliocene periglacial sand fluxes on the Antarctic continental margin. *Depositional Rec.* **7**, 564–581 (2021).
53. Cook, C. P. *et al.* Sea surface temperature control on the distribution of far-traveled Southern Ocean ice-rafted detritus during the Pliocene. *Paleoceanography* **29**, 533–548 (2014).
54. McKay, R. *et al.* The stratigraphic signature of the late Cenozoic Antarctic Ice Sheets in the Ross Embayment. *GSA Bull.* **121**, 1537–1561 (2009).
55. Sugden, D. & Denton, G. Cenozoic landscape evolution of the Convoy Range to Mackay Glacier area, Transantarctic Mountains: Onshore to offshore synthesis. *Geol. Soc. Am. Bull.* **116**, 840–857 (2004).
56. Verret, M. *et al.* Late Miocene onset of hyper-aridity in East Antarctica indicated by meteoric beryllium-10 in permafrost. *Nat. Geosci.* **16**, 492–498 (2023).
57. Weertman, J. Stability of the junction of an ice sheet and an ice shelf. *J. Glaciol.* **13**, 3–11 (1974).
58. Conte, R. *et al.* Bottom current control on sediment deposition between the Iselin Bank and the Hillary Canyon (Antarctica) since the late Miocene: An integrated seismic-oceanographic approach. *Deep Sea Res. Part Oceanogr. Res. Pap.* **176**, 103606 (2021).
59. Hill, D. J., Bolton, K. P. & Haywood, A. M. Modelled ocean changes at the Plio-Pleistocene transition driven by Antarctic ice advance. *Nat. Commun.* **8**, 14376 (2017).

60. Diekmann, B. *et al.* Detrital sediment supply in the southern Okinawa Trough and its relation to sea-level and Kuroshio dynamics during the late Quaternary. *Mar. Geol.* **255**, 83–95 (2008).
61. Prins, M. A. *et al.* The Late Quaternary Sedimentary Record of Reykjanes Ridge, North Atlantic. *Radiocarbon* **43**, 939–947 (2001).
62. Jimenez-Espejo, F. J. *et al.* Paleoenvironmental changes in the western Mediterranean since the last glacial maximum: High resolution multiproxy record from the Algero–Balearic basin. *Palaeogeogr. Palaeoclimatol. Palaeoecol.* **246**, 292–306 (2007).
63. Grygar, T. M., Mach, K. & Martinez, M. Checklist for the use of potassium concentrations in siliciclastic sediments as paleoenvironmental archives. *Sediment. Geol.* **382**, 75–84 (2019).
64. Mesa-Fernández, J. M. *et al.* Paleocirculation and paleoclimate conditions in the western Mediterranean basins over the last deglaciation: New insights from sediment composition variations. *Glob. Planet. Change* **209**, 103732 (2022).
65. Pérez, L. F. *et al.* Early to middle Miocene ice sheet dynamics in the westernmost Ross Sea (Antarctica): Regional correlations. *Glob. Planet. Change* **216**, 103891 (2022).
66. Richter, T. O. *et al.* The Avaatech XRF Core Scanner: technical description and applications to NE Atlantic sediments. *Geol. Soc. Lond. Spec. Publ.* **267**, 39–50 (2006).
67. Elliot, D. H. & Fleming, Thomas. H. Chapter 2.1b Ferrar Large Igneous Province: petrology. in *Volcanism in Antarctica: 200 Million Years of Subduction, Rifting and Continental Break-up* (eds Smellie, J. L., Panter, K. S. & Geyer, A.) (Geological Society of London, 2021). doi:10.1144/M55-2018-39.
68. Bertram, R. Reconstructing the East Antarctic ice sheet during the Plio-Pleistocene using geochemical provenance analysis. PhD Dissertation (Imperial College London, 2018) doi:10.25560/83552.

69. Struve, T. *et al.* Neodymium isotopes and concentrations in aragonitic scleractinian cold-water coral skeletons - Modern calibration and evaluation of palaeo-applications. *Chem. Geol.* **453**, 146–168 (2017).
70. Lambelet, M. *et al.* Neodymium isotopic composition and concentration in the western North Atlantic Ocean: Results from the GEOTRACES GA02 section. *Geochim. Cosmochim. Acta* **177**, 1–29 (2016).
71. Tanaka, T. *et al.* JNdi-1: a neodymium isotopic reference in consistency with LaJolla neodymium. *Chem. Geol.* **168**, 279–281 (2000).
72. Weis, D. *et al.* High-precision isotopic characterization of USGS reference materials by TIMS and MC-ICP-MS. *Geochem. Geophys. Geosystems* **7**, (2006).
73. Meyers, S., Malinverno, A., Hinnov, L., Zeeden, C. & Moron, V. astrochron: A Computational Tool for Astrochronology. (2019). https://CRAN.R-project.org/package=astrochron

Supplementary Figures

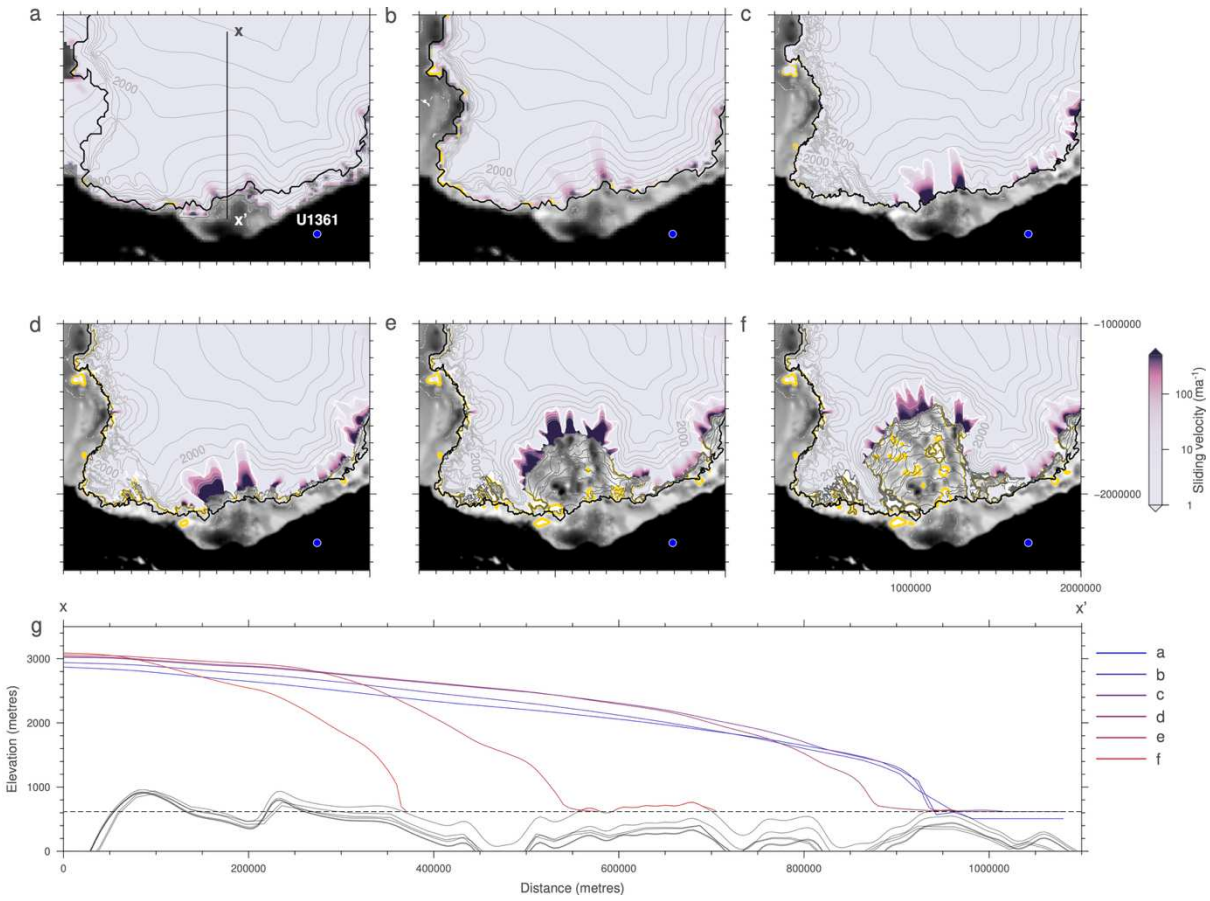
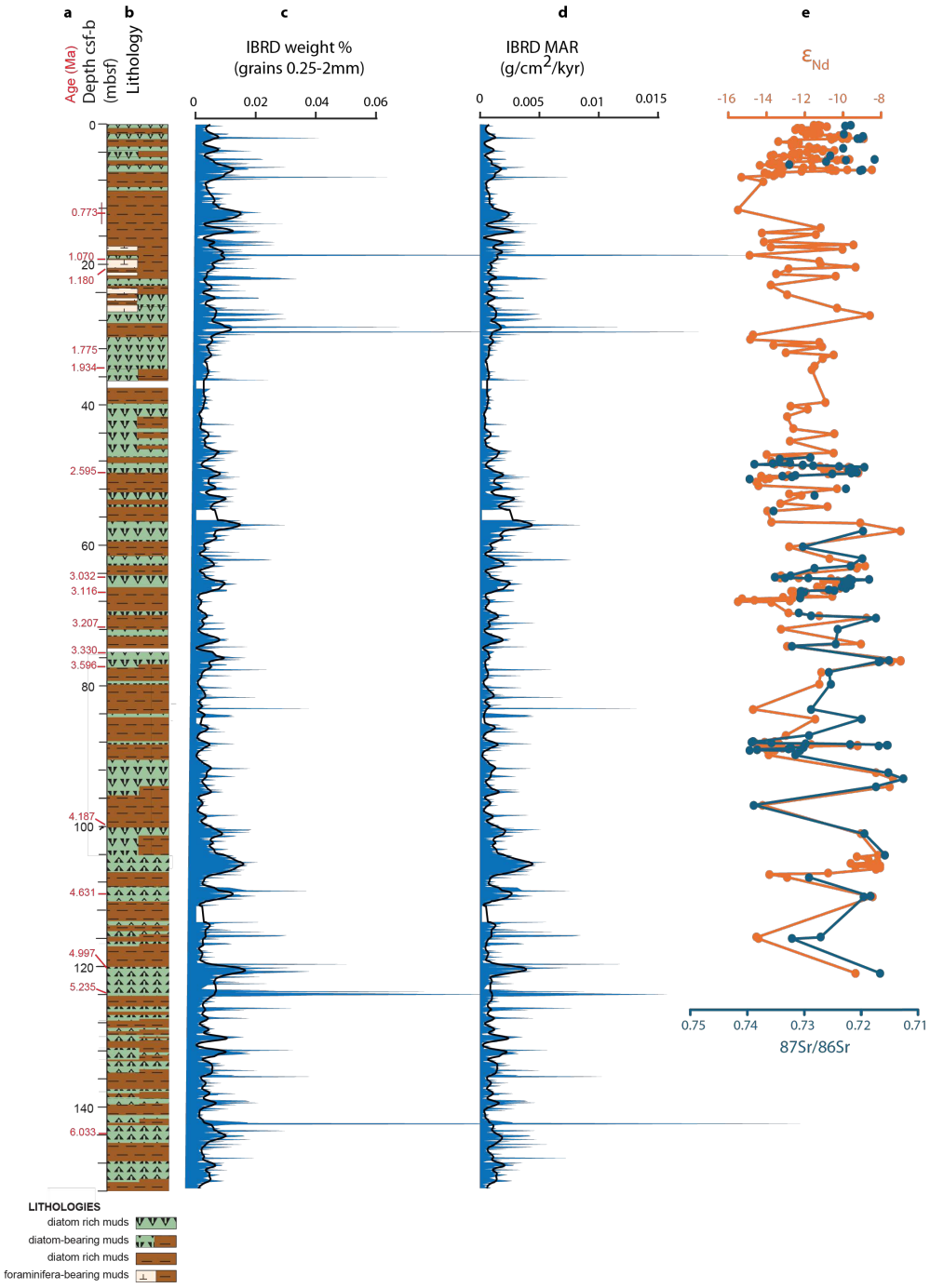


Figure S1: Same as Figure 1, but without the overlaid locations of the Jurassic Ferrar Large Igneous Province (FLIP; green areas), which partially obscured the colour ramp showing basal velocity of the simulated ice sheet.



748

749 **Figure S2: a) Magneto-stratigraphic age constraints[27] tied to the 2020 Geological**

750 **Timescale[48] (red numbers); b) Lithostratigraphic column of IODP Site U1361, with c)**

751 **IBRD weight percent versus depth, and d) IBRD MAR plotted versus depth. Blue filled**

752 **curve is the raw data, and black line is a 20-point robust loess smooth that assigns zero**

753 **weight to data outside six mean absolute deviations. e) ε_{Nd} values (orange) and $^{87}Sr/^{86}Sr$**

754 **ratios (dark blue) versus depth.**

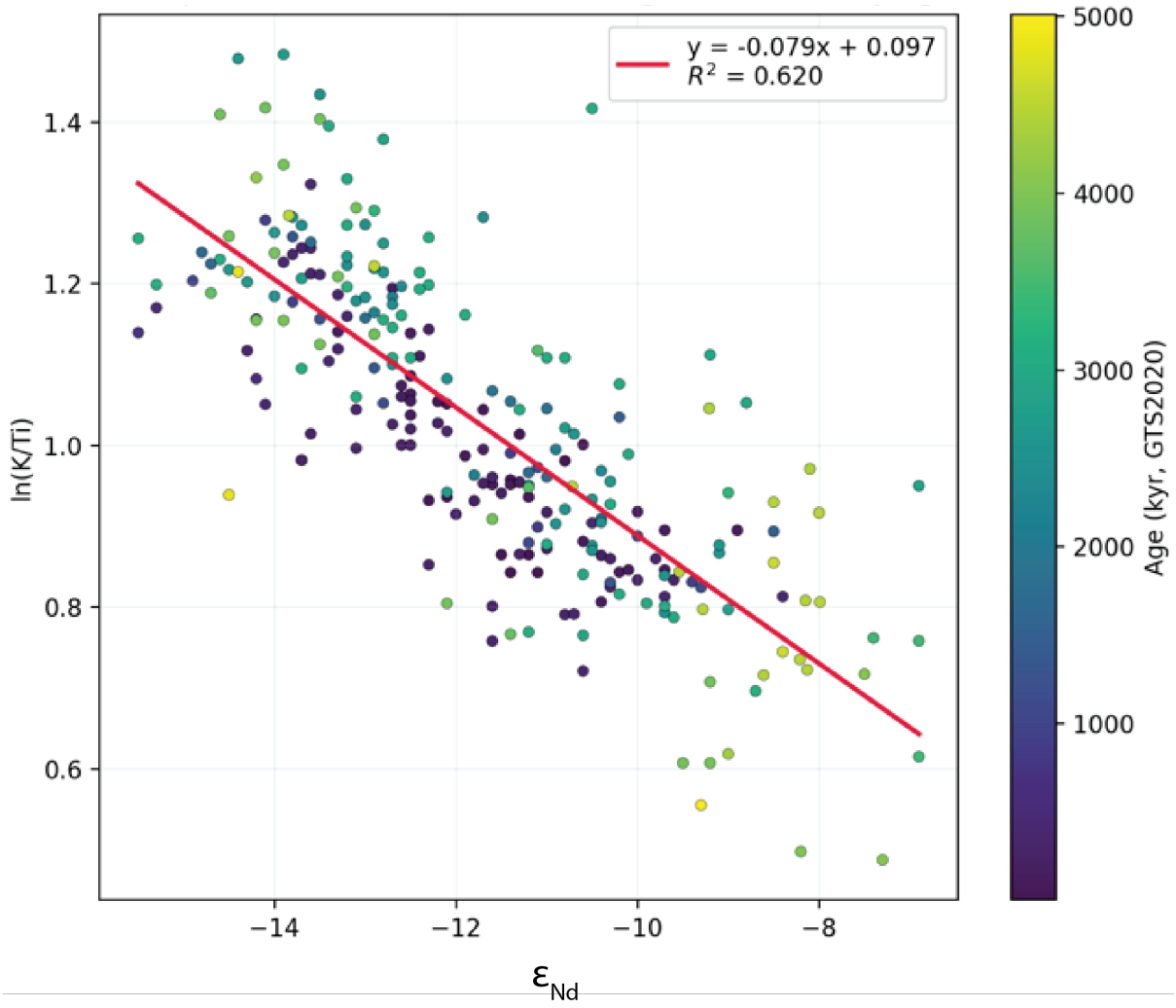


Figure S3: Cross plot of ln(K/Ti) vs ε_{Nd}. Correlation is based on resampling of ε_{Nd} values to nearest neighbour ln(K/Ti) values by age.

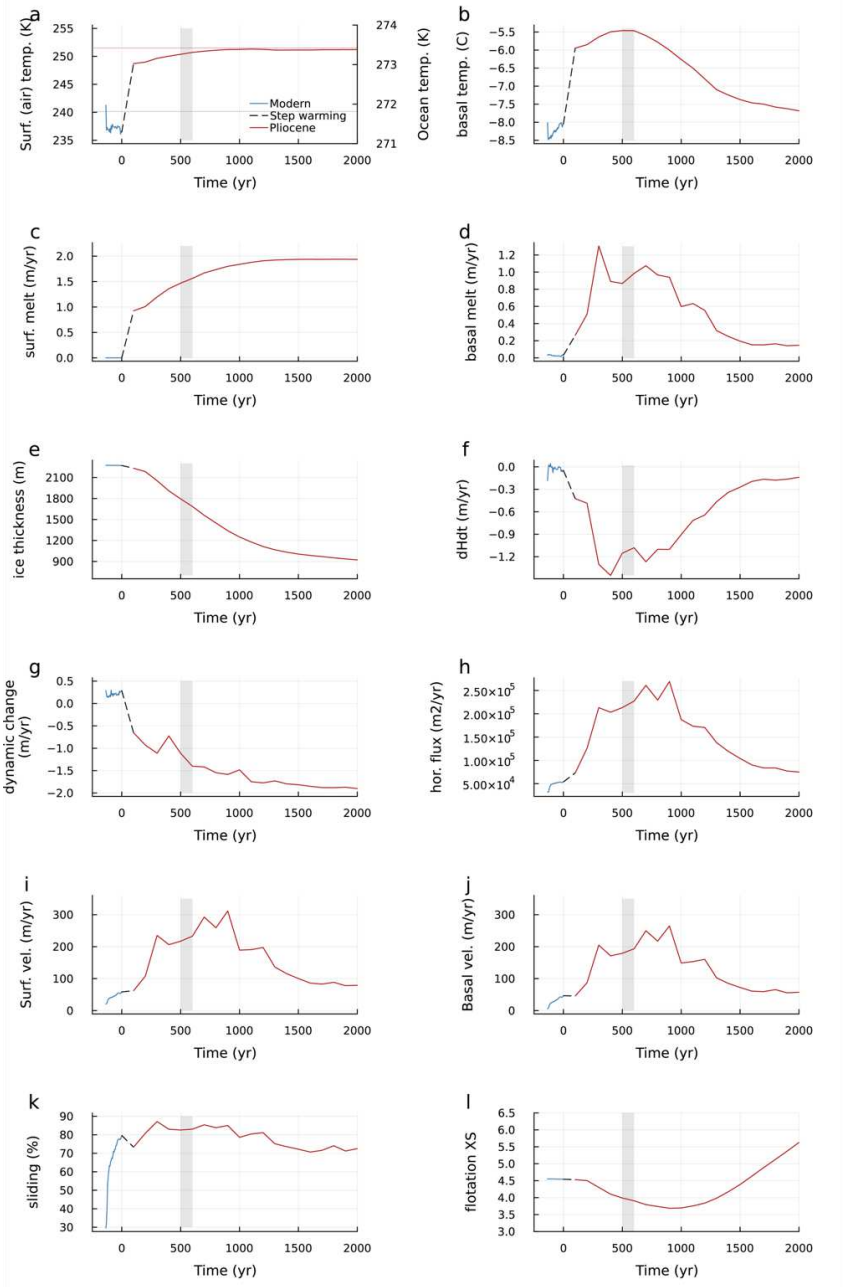


Figure S4: Mechanics of ice sheet retreat. Modelled ice margin retreat in the Wilkes Subglacial Basin is driven by warmer imposed atmospheric (solid lines) and oceanic (dotted lines) temperatures (a) leading to an abrupt warming at the ice sheet bed (b). These thermal changes are associated with higher rates of surface (c) and basal (d) melt,

that contribute to ice sheet thinning (e). The total rate of thickness change (f) is also influenced by dynamic thinning (g), which combined with the mass balance components drives changes in horizontal ice flux (discharge, h). Surface (i) and basal (j) velocities mirror changes in ice flux. The proportion of flow by basal sliding appears only moderately impacted in the area-averaged case (k). Flotation excess (l) denotes the ice overburden thickness as a proportion of the area-averaged flotation thickness. Grey vertical bars identify the time when the area-averaged ice shelf area first exceeds the area of grounded ice. Black dashed lines connect the end state of the 'modern' simulation with the first output (100 years) of the 'Pliocene' simulation.

Acknowledgements

This research used data and samples provided by the International Ocean Discovery Program (IODP), which is sponsored by the US National Science Foundation (NSF) and participating countries under the management of Joint Oceanographic Institutions. R.M. and G.G. were funded by Royal Society of New Zealand Marsden Fund contract MFP-VUW2207. RM, NG, EK, GG, RL, GD, CR were supported by Ministry of Business, Innovation and Employment, contracts RTVU2206 (Our Changing Coast) and ANTARCTICANZ2504 (Antarctic Science Platform). SRM was supported by the Heising-Simons Foundation (Award 2021-2797 to S.R.M.), a Guggenheim Fellowship, and a University of Wisconsin-Madison research/sabbatical leave. RA was supported by a Kristian Gerhard Jebsen PhD Scholarship to RA. TvdF was supported by NERC (NE/H025162/1, NE/H014144/1, NE/W000172/1 and NE/X009394/1). DJW was supported by a Natural Environment Research Council independent research fellowship (NE/T011440/1). CE and FJ were funded by the Spanish Ministry of

Science, Innovation and Universities project PID2021-126495NB-C31, cofounded by the European Union through FEDER funds.

Author contributions

Conceptualization: RM, TvdF, NG, MP, EK, SM. Data curation: RM, TvdF, MP, GG, NT, RA, DW, FJ, JM. Formal analysis: RM, NG, EK, SM, NS. Funding acquisition: RM, TvdF. Methodology: RM, TvdF, NG, MP, EK, SM. Software: SM, NS. Visualization and figures: RM, SM, NG, EK. Writing—original draft: RM. Writing—review and editing: all authors.

Supplementary Files

This is a list of supplementary files associated with this preprint. Click to download.

- ALLDATAGTS2020.xlsx